

1      **Effects of pre-existing structures on the seismicity of**  
2      **the Charlevoix Seismic Zone**

3      **Oluwaseun Idowu Fadugba<sup>1</sup>, Eunseo Choi<sup>1</sup>, and Christine A. Powell<sup>1</sup>**

4      <sup>1</sup>Center for Earthquake Research and Information, The University of Memphis, Memphis, TN 38152

5      **Key Points:**

- 6      • The CSZ seismicity and stress orientations are the combined effects of the rift faults  
7      and the impact *OF:~~erater~~structure*.
- 8      • Planar faults we considered can explain the observed seismicity but only 50% of  
9      the stress rotation.
- 10     • *OF:~~A~~crater*An impact structure four times less elastically stiff than the surround-  
11     ing crust can explain the seismicity in the CSZ.

12      **Abstract**

13      The Charlevoix Seismic Zone (CSZ) ~~occurs is located~~ along the early Paleozoic St. Lawrence  
 14      rift zone in southeastern Quebec at the location of a major Devonian impact ~~erater struc-~~  
 15      ~~ture~~. The ~~erater impact structure~~ superimposed major, steeply dipping basement faults  
 16      trending ~~approximately~~ N35°E. ~~Many Approximately 250~~ earthquakes are recorded  
 17      each year in the CSZ and are concentrated within and beneath the impact ~~erater struc-~~  
 18      ~~ture~~. ~~Some large magnitude Most M4+~~ earthquakes associated with the rift faults oc-  
 19      curred outside the ~~erater impact structure~~. Apart from the unique distribution of earth-  
 20      quakes in the CSZ, stress inversion of focal mechanisms shows stress rotations within the  
 21      CSZ, and in the CSZ relative to the stress orientation determined from borehole break-  
 22      outs. The primary goal of this research is to investigate the combined effects of the pre-  
 23      existing structures and regional stresses on earthquake activity and stress rotations in  
 24      the CSZ. We approach this using PyLith, a finite-element code for simulations of crustal  
 25      deformation. Adopting the results from recent hypocenter relocation and 3D tomogra-  
 26      phy studies, we modify the locations and dips of the rift faults and assess the effect of  
 27      the new fault geometries on stress distributions. We also discuss the effects of resolved  
 28      velocity anomalies. We find that the observed stress rotation is due to the combined ef-  
 29      fect of the rift faults and the ~~erater impact structure~~. 1D velocity models of the  
 30      CSZ with an embedded ~~erater impact structure~~ and a combination of 65°-40°-40° and  
 31      constant 70° fault dip models ~~for the three main rift faults~~ with a ~~very low~~ fric-  
 32      tion coefficient of 0.3 and cohesion of 0 MPa can explain the observed seismicity and more  
 33      than 50% of the stress rotations.

34      **1 Introduction**

35      The Charlevoix Seismic Zone (CSZ) is the most seismically active region in east-  
 36      ern Canada. The CSZ is within the ~~Cambro-Ordovician Late Precambrian~~ St. Lawrence  
 37      rift zone in southeastern Quebec and is overprinted by a Devonian impact ~~erater struc-~~  
 38      ~~ture~~ (Fig. 1). The impact ~~erater structure~~ has a radius of 28 km and is ~~45 approx-~~  
 39      ~~imately 12~~ km deep (Rondot, 1994). The ~~erater impact structure~~ has a more damaged  
 40      interior zone with a surface radius of 18 km (Fig. 1). The impact ~~erater structure~~ is  
 41      superimposed on three major rift faults trending N35°E and dipping to the southeast (An-  
 42      glin, 1984; Rondot, 1971). The CSZ ~~is considered to pose a high risk of seismic hazard has~~

43 a high seismic hazards due to its history of generating *OF:large*moderate to large earth-  
 44 quakes (Anglin, 1984; Lamontagne, 1999). Over 200 earthquakes are recorded each year  
 45 in the CSZ (Nuttli magnitude, mN *OF:mostly*  $\leq 3$ ) (Baird, McKinnon, & Godin, 2010)  
 46 and the hypocenters have a bimodal distribution with peaks at 10 and 22 km depths (Vla-  
 47 hovic, Powell, & Lamontagne, 2003). The vast majority of earthquakes in the CSZ oc-  
 48 cur within the volume bounded by the rift faults (Yu, Liu, Harrington, & Lamontagne,  
 49 2016) and those with greater magnitudes occur northeast of the *OF:erater*impact struc-  
 50 ture (Mazzotti & Townend, 2010) (Fig. 1).

51 Vlahovic et al. (2003) conducted a three-dimensional (3D) P-wave velocity study  
 52 of the CSZ. The tomography model shows several *OF:high-velocity*higher P velocity bod-  
 53 ies at mid-crustal depths. A significant fraction of the CSZ earthquakes occurs around  
 54 these *OF:high-velocity*higher P velocity bodies and some larger earthquakes occur along  
 55 the northern edges of the high velocity bodies.

56 A recent earthquake relocation and tomography study of Powell and Lamontagne  
 57 (2017) using a larger number of CSZ earthquakes gives a better constraint on the geome-  
 58 tries of these high-velocity bodies. In addition to the high-velocity bodies, Powell and  
 59 Lamontagne (2017) show that the relocated earthquakes are distributed along the rift  
 60 faults and thus define the geometry of the rift faults. They also conclude that the dip  
 61 of the northernmost rift fault is 65°SE while the two other major faults dip 40°SE.

62 Mazzotti and Townend (2010) determined the orientation of maximum principal  
 63 horizontal stress ( $SH_{max}$ ) from a stress inversion of focal mechanisms in ten seismic zones  
 64 in central and eastern North America including the CSZ. They found a clockwise rota-  
 65 tion of  $SH_{max}$  in the CSZ by about 32° relative to the regional  $SH_{max}$  orientation of 54°  
 66 determined from borehole breakouts (Mazzotti & Townend, 2010; Zoback, 1992). Maz-  
 67 zotti and Townend (2010) observed a number of relative stress rotations in  $SH_{max}$  de-  
 68 termined from different partitions of the earthquakes in the CSZ. The largest stress ro-  
 69 tation occurs in the cluster of earthquakes located southeast of the *OF:erater*impact struc-  
 70 ture midpoint relative to the earthquakes in the northwest of the *OF:erater*impact struc-  
 71 ture midpoint. Specifically,  $SH_{max}$  in the cluster of earthquakes located southeast of the  
 72 *OF:erater*impact structure midpoint shows about a 47° clockwise rotation whereas the clus-  
 73 ter located to the northwest has a  $SH_{max}$  that is compatible with the regional  $SH_{max}$  (Maz-  
 74 zotti & Townend, 2010) (Fig. 1).

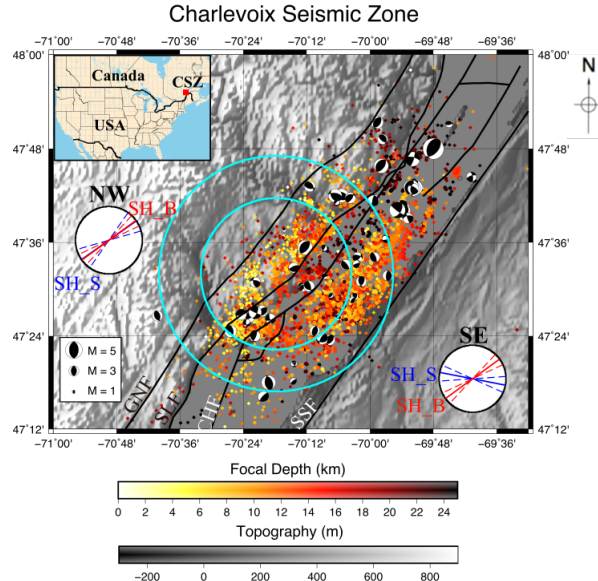


**Figure 1.** Topography<sup>OF:</sup>, bathymetry, and seismicity of the Charlevoix Seismic Zone (CSZ) as well as the locations of the impact <sup>OF:</sup>craterstructure (outer cyan circle) and the more damaged inner <sup>OF:</sup>craterimpact structure (inner cyan circle). Small circles <sup>OF:</sup>and the complete dataset for the years 1988-2011, respectively, and their colors represent the focal depths. The focal mechanisms are for the earthquakes used by Mazzotti and Townend (2010) for the stress inversion. Large circles labeled as NW and SE show orientations of  $SH_{max}$  from the stress inversion of focal mechanism ( $SH_S$ ) and from borehole breakout measurements ( $SH_B$ ) for the earthquake clusters northwest and southeast of the <sup>OF:</sup>craterimpact structure center. Solid black lines mark the rift faults known in the region: GNF, Gouffre Northwest Fault; SLF, Saint-Laurent fault; CHF, Charlevoix Fault; and SSF, South Shore Fault (Lamontagne, 1999; Rondot, 1971). The inset shows the location of the CSZ in eastern Canada. Earthquake <sup>OF:</sup>epicentershypocenters from the National Resources Canada catalog for the years 1988-2011.

75 Baird et al. (2010) explain the distribution of seismicity in the CSZ as products of  
 76 the interactions between the impact structure and the rift faults. Their numerical mod-  
 77 els for the rift faults and impact <sup>OF:</sup>craterstructure subjected to the regional stress show  
 78 increased differential stresses near the fault planes, which is consistent with the distri-  
 79 bution of the earthquakes. Stress solutions from their numerical models show greater dif-  
 80 ferential stress in the northeast of the <sup>OF:</sup>craterimpact structure, where <sup>OF:</sup>moremost of  
 81 the larger earthquakes occur, than in the southwest. However, their models could not

82 fully explain the  $\text{SH}_{\max}$  rotations in the CSZ relative to the regional  $\text{SH}_{\max}$ . Instead, they  
 83 addressed the observed stress rotations based on the discrepancy between the  $\text{SH}_{\max}$  from  
 84 the stress solutions in the seismogenic zone and the  $\text{SH}_{\max}$  inverted from the modeled  
 85 slips on the rift faults.

86 In this study, we present a new set of numerical models that can assess the impacts  
 87 ~~OF: on of~~ stress distribution due to fault geometry, frictional strengths of faults, elastic prop-  
 88 erties of the ~~OF: crater impact structure~~ and velocity models for the region. We then try  
 89 to correlate modeled stress distributions with the recently-relocated hypocenters (Pow-  
 90 ell & Lamontagne, 2017) and discuss implications for the non-uniform stress orientation  
 91 around the ~~OF: crater impact structure~~ that was previously recognized.

## 92 2 Model Setup

93 We create numerical models that include three major rift faults and the damaged  
 94 impact ~~OF: crater structure~~ (Fig. 2A). For this purpose, we use PyLith version 2.1.0 (Aa-  
 95 gaard, Kientz, Knepley, Strand, & Williams, 2015; Aagaard, Williams, & Knepley, 2015a,  
 96 2015b), an open-source finite element code for modeling dynamic and quasi-static tec-  
 97 tonic deformation. PyLith is suitable for the intended models because it can compute  
 98 elastic responses of a model involving multiple faults and material heterogeneities sub-  
 99 jected to various types of loading.

### 100 2.1 Model geometry

101 Our models are composed of three units, crust, ~~OF: crater impact structure~~ and rift  
 102 faults, reflecting a simplification of the geology of the region (Fig. 2A). The crust is a  
 103  $220 \times 220 \times 40$  km box with the ~~OF: crater impact structure~~ cut out. The impact ~~OF: crater struc-~~  
 104 ~~ture~~ is modeled as a spherical cap with a surface diameter of 60 km and a depth of 15  
 105 km.

106 The three rift faults have a strike of N35°E and are embedded in the crust layer  
 107 except for the top surface edge that is exposed on the surface. The three faults corre-  
 108 spond to the Gouffre ~~OF: NW~~ River, St. Laurent, and the Charlevoix faults (Fig. 1). Baird  
 109 et al. (2010) modeled the Gouffre River, St. Laurent, and the South Shore faults. They  
 110 did not model the Charlevoix fault. The locations of the rift faults relative to the ~~OF: crater im-~~  
 111 ~~pact structure~~ are based on geologic maps by Lamontagne (1999) and Rondot (1971).

112 We create two sets of models with different dip angles of the faults based on two pro-  
 113 posed geometries of the rift faults. One set has a uniform dip of 70°SE for all three faults  
 114 (Anglin, 1984; Baird et al., 2010) while the other has 65°, 40° and 40° for the three pla-  
 115 nar faults, from north to south, respectively (Powell & Lamontagne, 2017).

116 We conducted resolution tests in which the change in displacement and stress so-  
 117 lutions relative to a 1 km-resolution model are monitored as a function of element size  
 118 *OF:* (Fig. S1). Displacement was almost constant for 2 km or smaller element sizes. *OF:* We  
 119 use an element size of 4 km for more computational expensive models due to its  
 120 consistent displacement, but slightly higher stress solutions relative to the 2 km-reso-  
 121 lution model. We also observe edge effects by comparing a  $420 \times 420 \times 40$  km model  
 122 with the original  $220 \times 220 \times 40$  km model, finding that the seismogenic parts around  
 123 the *OF: crater impact structure* show consistent displacement and stress solutions for both  
 124 domain sizes. Based on this result, we choose the smaller domain for this study and set  
 125 the element size to be about 2 km. *OF:* We use an average computation time of about  
 126 16 days for fault models ( $\mu = 0.3$ ) with 2 km element size using 16 cores on the Uni-  
 127 versity of Memphis High Performance Computing cluster, except for the 65°-40°-40°  
 128 fault dip model, which took about twice longer to run for the same model time. We  
 129 do not clearly understand why this model is particularly slow and further analyzing  
 130 computational efficiency is beyond the scope of this paper. However, we use a mesh size  
 131 of 4 km to determine the effect of friction coefficient due to the expensive computa-  
 132 tion time of the models with  $\mu$  values of 0.1 and 0.2.

## 133 2.2 Initial and boundary conditions

134 Initial stresses are assumed to be lithostatic but due to the non-planar geometry  
 135 of the *OF: crater impact structure*, computing initial lithostatic equilibrium stresses is not  
 136 trivial. We first compute lithostatic stresses based on the density distribution from an  
 137 adopted velocity model for the CSZ (Table 1) and use it as an initial stress distribution.  
 138 We then use this stress solution as the true initial stress conditions. We verify that this  
 139 two-step approach leads to an initial stress field perfectly balancing the gravitational body  
 140 force by observing that the initial vertical displacements are uniformly zero.

141 Velocities are prescribed on the sides perpendicular to the  $x$ -axis (Fig. 2A) while  
 142 the  $y$ -perpendicular sides and the bottom boundary are free-slip and the top boundary

is traction-free. Rather than applying velocities oblique to the sides, we rotate the model domain such that the  $x$ -axis is oriented to N55°E, the regional  $\text{SH}_{\max}$  direction (Zoback, 1992) (Fig. 2B). We apply a 1 m/yr compressive velocity in the  $x$ -axis direction. The magnitude of boundary velocity does not represent any tectonic loading in the continental interiors but has the sole purpose of increasing the differential stress ( $\sigma_D = \sigma_1 - \sigma_3$ ). Noting that *OF: most earthquakes in the crater occur near 10 km depth* the distribution of earthquakes within the impact structure has a peak at 10 km (Baird et al., 2010; Powell & Lamontagne, 2017), we increase the boundary displacement until  $\sigma_D$  reaches 706 MPa at 10 km depth based on Byerlee's law,  $\tau = 50 \text{ MPa} + 0.6 \sigma_n$  (Byerlee, 1978).  $\sigma_3$  corresponds to the lithostatic stress. Lithostatic (compressive) stress is negative. *OF: We assume the absence of pore-fluid pressure along the rift faults (Fig. S2).*

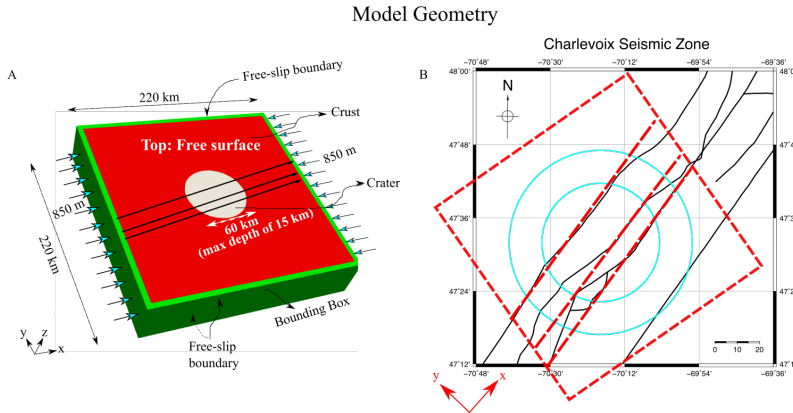


**Figure 2.** (A) Model domain with the *OF: crater impact structure* (gray) and crust (red). The three rift faults (black lines), dimensions, boundary conditions and the total amount of displacement are annotated. The outer 10 km-thick layer of crust (green) is added to contain fault edges within the domain, a requirement by PyLith. (B) The orientation of the model domain (red dotted box) and the associated coordinate axes (red arrows) relative to the geographic reference frame. The red dotted box is not the actual model domain but just a box that shows its "orientation." Cyan circles on the geographic map show the inner and outer *OF: crater impact structure* boundaries and black solid lines trace rift faults (see Fig. 1).

### 2.3 Elastic moduli from velocity models

We assume linear elasticity for both crust and *OF: crater impact structure*. To obtain elastic moduli and density distributions, we consider three regional velocity mod-

157    els and one recent model based on local earthquake tomography (Powell & Lamontagne,  
 158    2017). The regional models are for the Saguenay region in Quebec (Somerville, McLaren,  
 159    Saikai, & Helmberger, 1990), the 1D standardized halfspace velocity model of eastern  
 160    Canada (Lamontagne, 1999), and the 1D velocity model derived from *OF: seismic refra-*  
 161    *ction studies a simultaneous inversion of hypocenters and velocities of the CSZ* (Lamon-  
 162    tagne, 1999) (Fig. 3).

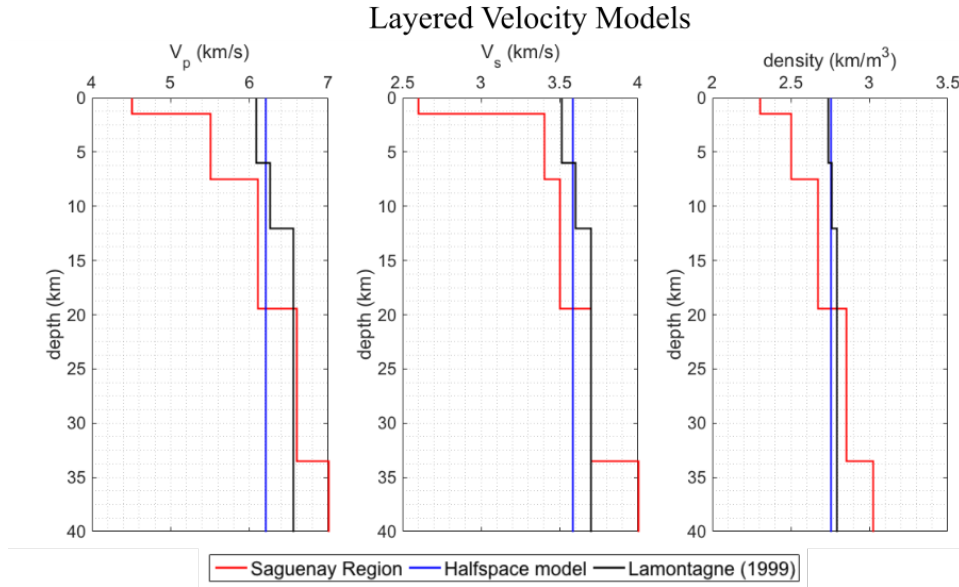


**Figure 3.** Velocity models used in this study. Red, blue and black lines are velocity models for the Saguenay region (Somerville et al., 1990), *OF: a standardized velocity the Geological Survey of Canada (GSC) standard velocity model* of Eastern Canada (Lamontagne, 1999) and the *OF: Canadian Shield (North Shore)* velocity model of CSZ (Lamontagne, 1999).

163    We also consider a non-uniform distribution of density and elastic moduli inferred  
 164    from the 3D  $V_p$  and  $V_s$  tomography model by Powell and Lamontagne (2017), of which  
 165     $V_p$  and  $V_s$  variations for the depth range from 12 to 14 km are shown in Fig. 4. The to-  
 166    mography has a block size of 2 km and velocity features with a dimension of 6 km can  
 167    be resolved. Since this tomography solution does not cover the entire study area, we as-  
 168    sume a halfspace velocity model (Lamontagne, 1999) outside of the tomography cover-  
 169    age. Smooth transition between the tomography model and the half-space model is achieved  
 170    by linear interpolation. Densities ( $\rho$ ) are computed according to Gardner's principle (Gard-  
 171    ner, Gardner, & Gregory, 1974):  $\rho = 0.31V_p^{0.25}$ , where  $V_p$  is the P-wave velocity in m/s  
 172    and density is given as g/cm<sup>3</sup>.

173 For simplicity, we assume that the *OF: crater impact structure*'s bulk and shear mod-  
 174uli are a certain fraction of those of the crust (e.g., Baird et al., 2010). Similarly, the den-  
 175sity of the *OF: crater impact structure* is reduced by 10 % from that of the 1D velocity mod-  
 176els over the corresponding depth range *OF: to model a damaged crustal rock, but the*  
 177*model results were insensitive to other amounts of reduction as seen in Fig. S3 in the*  
 178*supplementary information.*

### Tomography Models

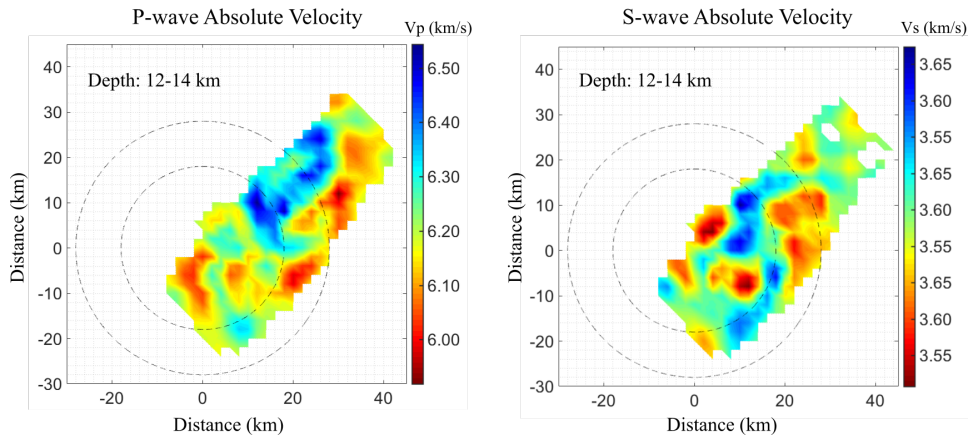


**Figure 4.** Variation of  $V_p$  and  $V_s$  at the depths from 12 to 14 km from the 3D seismic tomographic model by Powell and Lamontagne (2017).

#### 2.4 Treatment of rift faults

We treat the rift faults as cohesive-frictional planes, on which slip vectors are not prescribed but determined by the model. In order to create relative motions across the rift fault planes, PyLith decouples the motion of the two sides of the faults by inserting cohesive cells on the fault surfaces. We assign a coefficient of static friction ( $\mu$ ) and the cohesion ( $C$ ) on the fault. We assume that  $\mu$  and  $C$  are uniform on the fault planes in each model but investigate the consequences of varying  $\mu$  from 0.1 to 0.6 at a constant  $C$  of 0 MPa. *OF: We compute a series of models in which the rift faults dip at 70° but their cohesion ( $C$ ) is varied systematically at a constant friction coefficient ( $\mu$ ) of 0.3. We use six models with cohesion values of 0, 3, 5, 10, 20 and 30 MPa (Fig. S4). Cohesion values less than 5 MPa could explain the spatial distribution of observed seismicity in the CSZ.* We choose a cohesion of 0 MPa based on a report that a zero cohesion is sufficient for most pre-existing faults (Marone, 1995).

The reference model (SNFR25) has the geometry described above but without the rift faults. This is equivalent to a model with infinitely strong faults. The initial stress state is close to the initially assumed lithostatic stress after the nonplanar correction due to the *OF:eraterimpact structure*. We determine the percentage change in differential stress,  $\Delta\sigma'_D = 100(\sigma_D - \sigma_{D,ref})/\sigma_{D,ref}$ , and the change in the orientation of  $\text{SH}_{max}$ ,  $\Delta\phi_{\max} = \phi_{\max} - \phi_{\max,ref}$ , where  $\phi_{\max}$  denotes the orientation of the maximum principal stress ( $\sigma_1$ ). Since our model domain was rotated clockwise about the center of the *OF:eraterimpact structure* by  $35^\circ$ ,  $\phi_{\max}$  equal to zero should be understood as parallel to the regional stress field. Positive and negative values of  $\phi_{\max}$  correspond to anticlockwise and clockwise rotation from the direction of applied loading, respectively. *OF:In order to quantify the fitting between the simulated stress change and the earthquake hypocenters, we determine the percentage of hypocenters that fall within region of  $\Delta\sigma'_D \geq 0.5\%$ . We did not account for the uncertainty in hypocenter relocation and the effect of any along-strike variation in the fault dips in reality.*

## 2.5 Control Parameters

We create a series of models in which the following parameters are varied: dips of the rift faults, friction coefficients, *OF:eraterimpact structure*-crust elastic moduli ratios, and the velocity models. Two fault geometries for the CSZ are considered. One model has a dip angle of  $70^\circ\text{SE}$  for all three rift faults (Baird et al., 2010). The other assumes that the three faults have dip angles of  $65^\circ\text{SE}$ ,  $40^\circ\text{SE}$  and  $40^\circ\text{SE}$  from north to south (Powell & Lamontagne, 2017).

*OF:eraterImpact structure*-crust elastic moduli ratios tested are 0.25, 0.5 and 1.0. When the modulus ratio is 1.0, the *OF:eraterimpact structure* has the same velocity model as the crust. The friction coefficient,  $\mu$ , is varied from 0.1 to 0.6 at a constant cohesion of 0 MPa in one set of models. We assume that  $\mu$  and  $C$  are the same for the three rift faults and it is uniform on the fault planes, including the part of the faults within the *OF:eraterimpact structure* region.

Three velocity models are considered in this study: The 1D Saguenay velocity model (Somerville et al., 1990), the 1D CSZ velocity model (Lamontagne, 1999) and the 3D  $V_p$  and  $V_s$  tomography model (Powell & Lamontagne, 2017) (Figs. 3 and 4). When the tomography

**Table 1.** List of numerical models

Model	Velocity Model	Dip of Rift Faults	Moduli ratio	$\mu$	$C$	$K^*$ (MPa)	$G^*$ (MPa)
SNFR25	Saguenay Region <sup>1</sup>	No faults	0.25	0.3	0	55.7	32.7
SD70R25		70° – 70° – 70°	0.25	0.3	0	55.7	32.7
SD70R25V		70° – 70° – 70°	0.25	0.1-0.6	0	55.7	32.7
SD65R25		65° – 40° – 40°	0.25	0.3	0	55.7	32.7
SD70R50		70° – 70° – 70°	0.5	0.3	0	55.7	32.7
SD70R100		70° – 70° – 70°	1.0	0.3	0	55.7	32.7
LD70R25	1-D Model <sup>2</sup>	70° – 70° – 70°	0.25	0.3	0	60.0	35.7
TD70	Tomography <sup>3</sup>	70° – 70° – 70°	-	0.3	0	58.7	35.3

model is used, the *OF:eraterimpact structure*-crust moduli ratio becomes irrelevant. All the models presented in this paper are listed in Table 1.

### 3 Results

#### 3.1 Reference Model (SNFR25)

The effects of the weaker *OF:eraterimpact structure* are dominant in SNFR25.  $\sigma_D$  is smaller by 100s MPa in the *OF:eraterimpact structure* region relative to the surrounding crustal rock as shown by 5 and 10-km depth sections (Fig. 5A). The absolute value of  $\sigma_D$  is greater (i.e. is more negative) in the direction perpendicular to the applied loading than in the parallel direction. At depths below the *OF:eraterimpact structure* (i.e., depths  $\geq 15$  km),  $\sigma_D$  is more negative at the central region by about 300 MPa relative to the average  $\sigma_D$  at those depths (Fig. 5A). The higher negative value of  $\sigma_D$  at 15 km depth decreases to the average value at that depth within 20 km from the center of the model geometry. The effect of the *OF:eraterimpact structure* weakens at 20 km and eventually becomes insignificant at 25 km (Fig. 5A).

$\phi_{\max}$ , the orientation of  $\text{SH}_{\max}$ , shows a four-lobe pattern of alternating polarities around the *OF:eraterimpact structure* (Fig. 5B).  $\phi_{\max}$  uniformly approaches 0°, the loading direction, away from the *OF:eraterimpact structure* and also with depth (Fig. 5B). In the SE corner of the *OF:eraterimpact structure*,  $\phi_{\max}$  shows a maximum clockwise (i.e., negative) rotation of about 18.3° from the regional stress direction (5 km panel in Fig.

241 5B).  $\phi_{\max}$  at 5 km and 10 km depths is close to  $0^\circ$  within the *OF:eraterimpact structure*,  
 242 being subparallel to the regional stress orientation (Zoback, 1992).

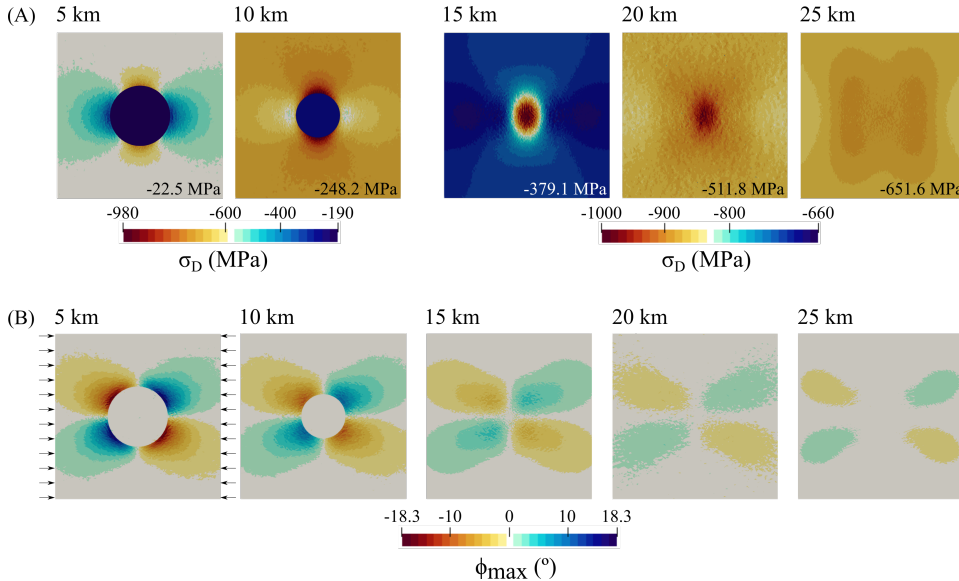


**Figure 5.** (A) Differential stress ( $\sigma_D$ ) and (B)  $\text{SH}_{\max}$  orientation ( $\phi_{\max}$ ) in the reference model (SNFR25) at different depths. The value of lithostatic stress at each depth is at the lower right corner of each depth slice in 5A. The arrows in 5B represent the loading direction for all models. Note the change in scale in 5A for depths greater than 10 km. Each figure is  $70 \times 70$  km.

### 243 3.2 Effects of rift faults and their dip

#### 244 3.2.1 SD70R25

245 Magnitudes of  $\sigma_D$  in SD70R25 are smaller in the *OF:eraterimpact structure* than  
 246 in the surrounding crust, as in the reference model, but also significantly modified by abrupt  
 247 changes in the vicinity of the rift faults (Fig. 6A).  $\sigma_D$  at a distance greater than 50 km  
 248 from the center of the *OF:eraterimpact structure* is similar to that of the reference model  
 249 at each depth.

250  $\phi_{\max}$  shows a four-lobe pattern of alternating polarities around the weaker *OF:eraterim-*  
 251 *pact structure* but modifications made by the faults are also clearly visible.  $\phi_{\max}$  in the  
 252 surrounding crust approaches  $0^\circ$  as distance from the *OF:eraterimpact structure*'s cen-  
 253 ter or depth increases (Fig. 6B).  $\phi_{\max}$  within the *OF:eraterimpact structure* is about  $-5^\circ$

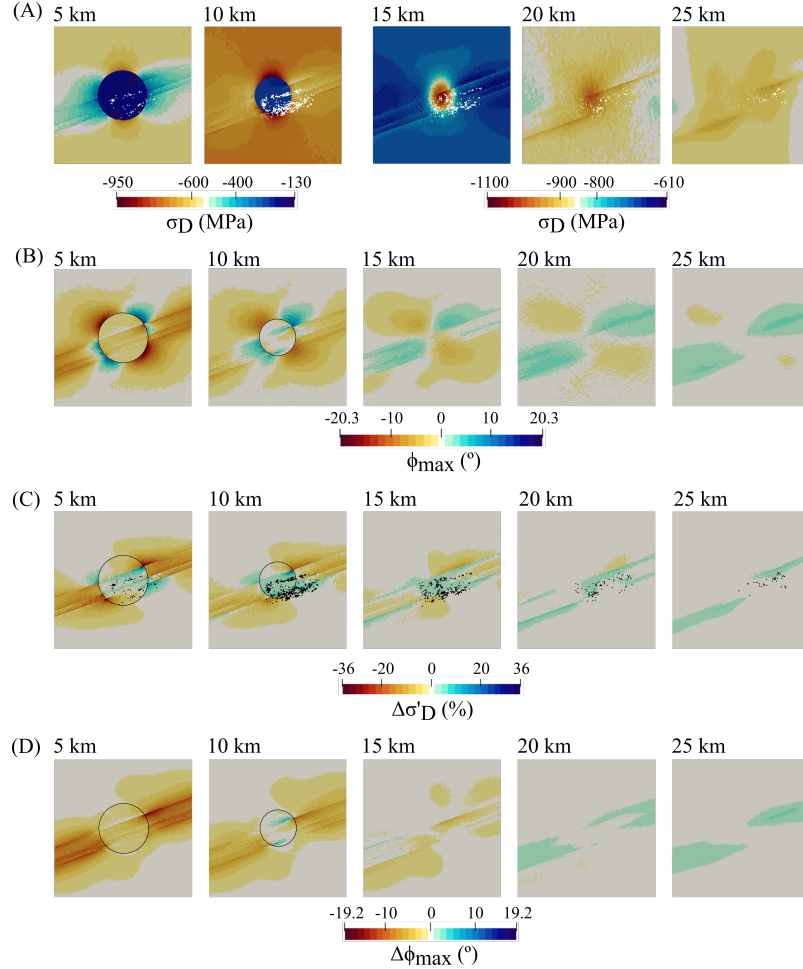


**Figure 6.** (A) Differential stress ( $\sigma_D$ ), (B)  $\text{SH}_{\max}$  orientation ( $\phi_{\max}$ ), (C) Percentage change in differential stress ( $\Delta\sigma'_D$ ) and (D) the change in  $\phi_{\max}$  ( $\Delta\phi_{\max}$ ) in SD70R25 model relative to SNFR25 at various depths. Note the change in scale in 6A for depths greater than 10 km. Earthquakes within 2 km of each depth slice are represented by black dots in 6C. *OF: The outline of the impact structure is represented as black circle.* Each figure is  $70 \times 70$  km.

at a depth of 5 km but is subparallel to the regional stress orientation at 10 km depth (Fig. 6B). The main effect of the rift faults is a  $5^\circ$  to  $15^\circ$   $\phi_{\max}$  clockwise rotation that persists along the faults at 5 and 10 km depths. The sense of near-fault  $\phi_{\max}$  rotations flips to anticlockwise at 10 km within the *OF: crater impact structure* and at depths below the *OF: crater impact structure* in the surrounding crust. The anticlockwise rotation also persists along the faults and has a magnitude of about  $5^\circ$ .

The distribution of positive  $\Delta\sigma'_D$  values, corresponding to increased differential stresses in SD70R25 relative to SNFR25, spatially overlaps with the seismicity in general and particularly well at 10 km (Fig. 6C). *OF:* About 70% of the hypocenters fall in region with  $\Delta\sigma'_D \geq 0.5\%$ . We superimpose the relocated hypocenters of earthquakes of Powell and Lamontagne (2017) that occurred within 2 km of each depth slice. The hypocenters are rotated clockwise by  $35^\circ$  about the center of the *OF:* eraterimpact structure in order for them to be consistent with the rotated model geometry. Some earthquakes fall in the region of negative  $\Delta\sigma'_D$  near the SW and NE boundary of the *OF:* eraterimpact structure at depths shallower than 15 km.

The  $\Delta\phi_{\max}$  maps in Fig. 6D show that the rift faults rotate  $\text{SH}_{\max}$  of SNFR25 further clockwise at 5 and 10 km depths by up to  $19^\circ$ . The effect of clockwise rotation due to the faults is diminished within the *OF:* eraterimpact structure and flips the sense of rotation to anticlockwise at 10 km (Fig. 6D). At depths below the *OF:* eraterimpact structure, the overall impact of the faults decrease everywhere.

Three vertical cross sections of  $\Delta\sigma'_D$  from the SD70R25 model are shown in Fig. 7. As marked on the 10-km depth slice of  $\Delta\sigma'_D$  (left panel in Fig. 7), they are all perpendicular to the fault strike. Two cross sections, 1 and 2, go through the central and marginal areas of the *OF:* eraterimpact structure but the cross section 3 does not intersect the *OF:* eraterimpact structure. Also plotted on these cross sections are the hypocenters of the region's earthquakes within 2 km from each cross section. Most of the earthquakes fall within regions of increased differential stress but some are associated with negative or negligible changes in differential stress. In the cross sections going through the *OF:* eraterimpact structure, the broad region between the northernmost and the southernmost fault shows positive  $\Delta\sigma'_D$ . In contrast, the relocated hypocenters exhibit well-defined linear trends as observed by Powell and Lamontagne (2017).

### 3.2.2 SD65R25

Correlation between the  $\Delta\sigma'_D$  distribution in SD65R25 and the observed seismicity is not as clear as in SD70R25 but shows more fine-scale correlation with the observed seismicity, especially at 10 km depth (Fig. 8). At 15 km depth, the region of positive  $\Delta\sigma'_D$  correlates with the earthquakes on the northernmost fault but the earthquakes on the middle rift fault fall in regions with negative  $\Delta\sigma'_D$ .

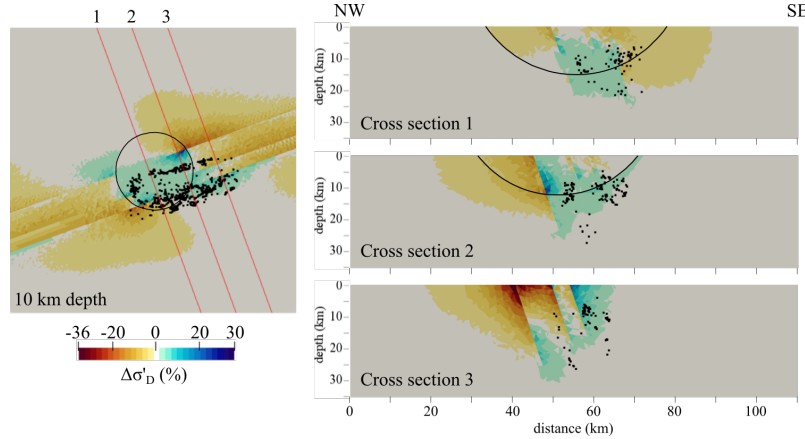


**Figure 7.** NW-SE cross sections through the percentage change in differential stress ( $\Delta\sigma'_D$ ) solution in the SD70R25 model. Earthquakes within 2 km of each cross section are represented by black dots. The three NW-SE cross sections are indicated on the 10-km depth slice showing earthquakes within 2 km of the depth slice. The outline of the *OF:eraterimpact structure* is represented as black circle and curved lines on the depth slice and cross sections, respectively. The depth slice is  $70 \times 70$  km centered on the impact *OF:eraterstructure*. Note the cross sections have the same color and length scales as the depth slice in 7A.

Greater clockwise rotations of  $\text{SH}_{\max}$  are found in SD65R25 than in SD70R25 at all depths (Fig. 8) although both models show the four-lobe pattern and magnitudes of  $\phi_{\max}$  decreasing with depth. Within the *OF:eraterimpact structure*, SD65R25 shows clockwise rotations of about  $5^\circ$  at 10 km depth and the counterclockwise rotation observed for model SD70R25 is seen only north of the northernmost fault because the other two faults barely cross the *OF:eraterimpact structure* region at this depth due to their shallower dip (Fig. 8). In the surrounding crust close to the rift faults,  $\phi_{\max}$  rotates clockwise by  $5^\circ$  to  $16.3^\circ$  relative to the regional stress direction (Fig. 8). Counterclockwise rotation of  $\phi_{\max}$  relative to the regional  $\text{SH}_{\max}$  extends to the northeast and southwest of the *OF:eraterimpact structure* in the fault-bounded region.

When compared to  $\text{SH}_{\max}$  orientations in the reference model, SD65R25 shows greater clockwise rotations of  $\phi_{\max}$  by up to  $20^\circ$  near the rift faults and the northeastern boundary of the *OF:eraterimpact structure* at 10 km depth (Fig. 8). These values of  $\Delta\phi_{\max}$  are greater than those of SD70R25 and thus can be attributed to the shallower dips of the faults in SD65R25.

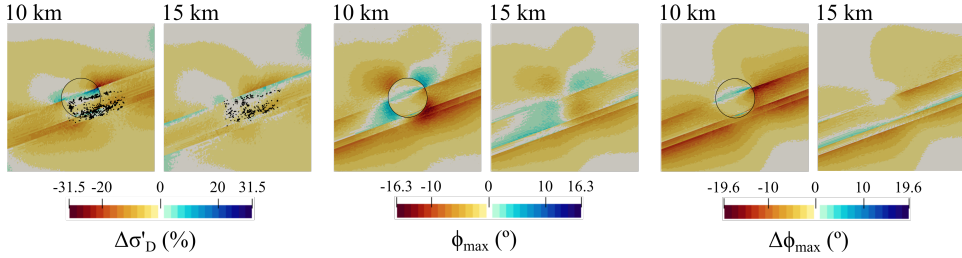


**Figure 8.** Percentage change in differential stress ( $\Delta\sigma'_D$ ), SH<sub>max</sub> orientation ( $\phi_{max}$ ) and the change in  $\phi_{max}$  ( $\Delta\phi_{max}$ ) at 10 and 15 km depths from the SD65R25 model. Earthquakes within 2 km of each depth slice are represented by black dots in 8A. *OF: The outline of the impact structure is represented as black circle.* Each figure is 70 × 70 km.

The region of increased differential stress in SD65R25 exhibits well-defined linear trends near the rift faults, and thus gives a better explanation for the narrow and well-defined seismicity near the *eraterimpact structure*, even though the overall percentage of the hypocenters that fall in region with  $\Delta\sigma'_D \geq 0.5\%$  is about 25%. (Fig. 9). The SD65R25 model shows a region of negative  $\Delta\sigma'_D$  between the observed seismicity on the northernmost and southernmost faults. The earthquakes on the middle rift fault and most of the earthquakes on the southernmost fault outside the *eraterimpact structure* fall in regions with negative  $\Delta\sigma'_D$  (Fig. 9).

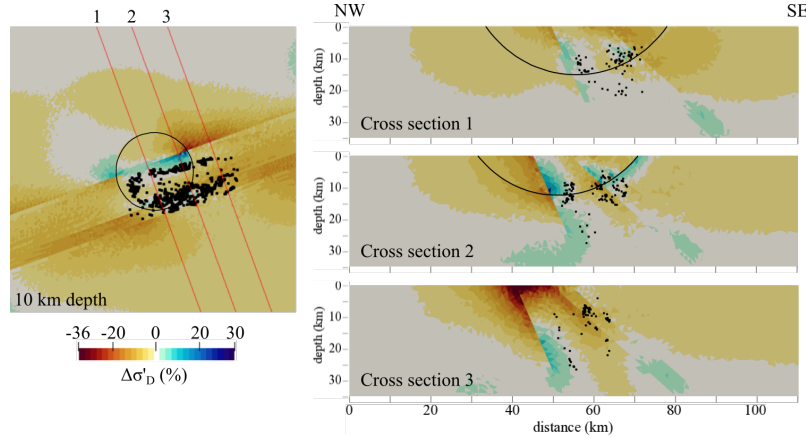


**Figure 9.** Same as Fig. 7 but for SD65R25 model.

### 3.3 Effects of the weakness of the damaged *OF:eraterimpact structure* zone

Two models with the rift faults dipping at  $70^\circ$  are constructed such that the ratio of elastic moduli of the *OF:eraterimpact structure* to that of the surrounding crust are 0.5 (SD70R50) and 1.0 (SD70R100), respectively.

#### 3.3.1 SD70R50

While the effects of the *OF:eraterimpact structure* and rift faults are still clear and consistent, SD70R50 values of  $\Delta\sigma'_D$  are mostly negative with some exceptions at 10 km depth amounting to about a 10 % increased stress (Fig. 10A). The region of positive  $\Delta\sigma'_D$  in the SD70R50 model overlaps with the hypocenters only in the southeast corner of the *OF:eraterimpact structure* boundary and the southernmost rift fault (i.e., the Charlevoix fault) at 5 km depth *OF*, *amounting to about 45% of the hypocenters in region with  $\Delta\sigma'_D \geq 0.5\%$* . (Fig. 10A). The spatial correlation of seismicity with increased  $\sigma_D$  relative to the reference model is stronger at 10 km depth.

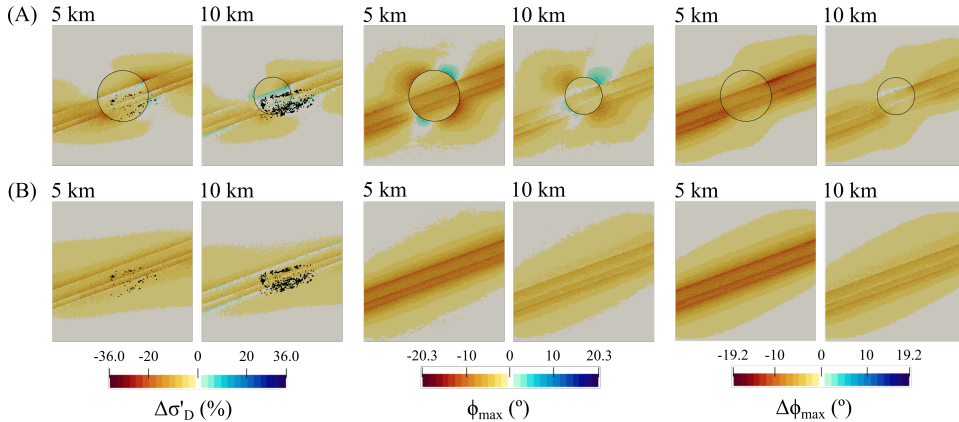


**Figure 10.** Same as Fig. 8 but for the models with different *OF:eraterimpact structure*-crust elastic moduli ratios: (A) SD70R50 and (B) SD70R100.

$\phi_{\max}$  plots show the four-lobe pattern of alternating polarities and shows the effects of the rift faults. The maximum value of  $\phi_{\max}$  is about  $13^\circ$  (Fig. 10A). The  $\Delta\phi_{\max}$  maps in Fig. 10A show that the rift faults rotates the  $\phi_{\max}$  in the reference model at 5 and 10 km depths up to  $16.5^\circ$ . The value of  $\Delta\phi_{\max}$  decreases to almost zero at 15 km depth, and is anticlockwise up to  $-3^\circ$  at 20 and 25 km depths.

332            **3.3.2 SD70R100**

333          $\Delta\sigma'_D$  and  $\phi_{\max}$  only exhibit the effects of the rift faults since the ~~OF: erater impact~~  
 334         structure and the crust have the same elastic moduli in model SD70R100 (Fig. 10B).

335         Positive  $\Delta\sigma'_D$  values in SD70R100 are seen only at a depth of 10 km and their dis-  
 336         tribution does not fit the observed seismicity (Fig. 10B). ~~OF: About 23% of the hypocen-~~  
 337         ters fall in region with  $\Delta\sigma'_D \geq 0.5\%$ .  $\Delta\sigma'_D$  correlates with observed seismicity below  
 338         15 km except for some earthquakes in the northern cluster. However, the model predicts  
 339         earthquakes throughout the entire length of the rift faults at and below 15 km depth.  
 340         Figures that shows all the depth slices are in the supplementary materials (Fig. S5). ~~OF: The~~  
 341         result of a model with an intermediate moduli ratio of 0.75 is somewhat between the  
 342         SD70R50 and SD70R100 models (Fig. S6).

343         The distribution of  $\phi_{\max}$  values lacks the four-lobe pattern and is negative in the  
 344         vicinity of the rift faults at 5 and 10 km depth: i.e.,  $\phi_{\max}$  values are rotated clockwise  
 345         relative to the regional  $SH_{\max}$  (Fig. 10B). The values of  $\phi_{\max}$  range from  $2^\circ$  (25 km depth)  
 346         to  $12.8^\circ$  (5 km depth).  $\phi_{\max}$  decreases to  $0^\circ$  at about 50 km from the center of the model  
 347         along the direction perpendicular to the fault strike.

348         The maximum value of  $\Delta\phi_{\max}$  is  $12.8^\circ$  and, being indistinguishable from  $\phi_{\max}$ , sig-  
 349         nifies that the  $\Delta\phi_{\max}$  values in SD70R100 are controlled by the rift faults (Fig. 10B).  
 350         The value of  $\Delta\phi_{\max}$  decreases to almost zero at 15 km depth, and becomes anticlock-  
 351         wise in the fault region at 20 and 25 km.

352            **3.4 Effects of fault strength (SD70R25V)**

353         We compute  $\sigma_D$  and  $\phi_{\max}$  in a series of models in which the rift faults dip at  $70^\circ$   
 354         but their friction coefficient ( $\mu$ ) is varied systematically at a constant cohesion of 0 MPa.  
 355         We assume that the fault parameters are the same for each rift fault and uniform through-  
 356         out the fault surfaces.  $\mu$  varies from 0.1 to 0.6 with an interval of 0.1. We use a mesh  
 357         resolution of 4 km for SD70R25V models due to the expensive computation time at  $\mu$   
 358         values of 0.1 and 0.2. Aside from the change in the friction coefficient and the mesh res-  
 359         olution, the six models computed are the same as SD70R25.  $\Delta\sigma'_D$  and  $\phi_{\max}$  computed  
 360         for these models are plotted in Fig. 11, which shows 10 km depth sections because of the  
 361         high number of earthquakes within 2 km from that depth.

Magnitudes of  $\Delta\sigma'_D$  decrease as  $\mu$  increases (Fig. 11A) because the model behaviors must approach those of the no-fault model as fault strength increases. When  $\mu$  values are 0.1 and 0.2, the area of positive  $\Delta\sigma'_D$  regions does not cover the entire observed seismicity<sup>OF:</sup>, with about 3% and 24% of the hypocenters in region with  $\Delta\sigma'_D \geq 0.5\%$ , respectively. The regions of positive  $\Delta\sigma'_D$  for  $\mu$  values equal to 0.3 and 0.4 show better spatial correspondence with the seismicity of the CSZ. However, the model with  $\mu = 0.4$  predicts positive Coulomb stress changes along the entire length of the rift faults, which is contrary to the limited spatial extent of the observed seismicity. <sup>OF:</sup>Also, about 66% of the hypocenters in the model with  $\mu$  of 0.3 fall within region of  $\Delta\sigma'_D \geq 0.5\%$ , compare to a value of 35% when  $\mu$  is 0.4. However, when we consider region with  $\Delta\sigma'_D \geq 0\%$ , the percentage increases to 82% when  $\mu$  of 0.4 compare to 73% in the model with  $\mu$  of 0.3.  $\Delta\sigma'_D$  approaches zero when  $\mu$  values are 0.5 and 0.6, for which the faults are locked. <sup>OF:</sup>The percentage of hypocenters in region with  $\Delta\sigma'_D \geq 0.5\%$  reduces to 1.4% and 0% when  $\mu$  values are 0.5 and 0.6, respectively.

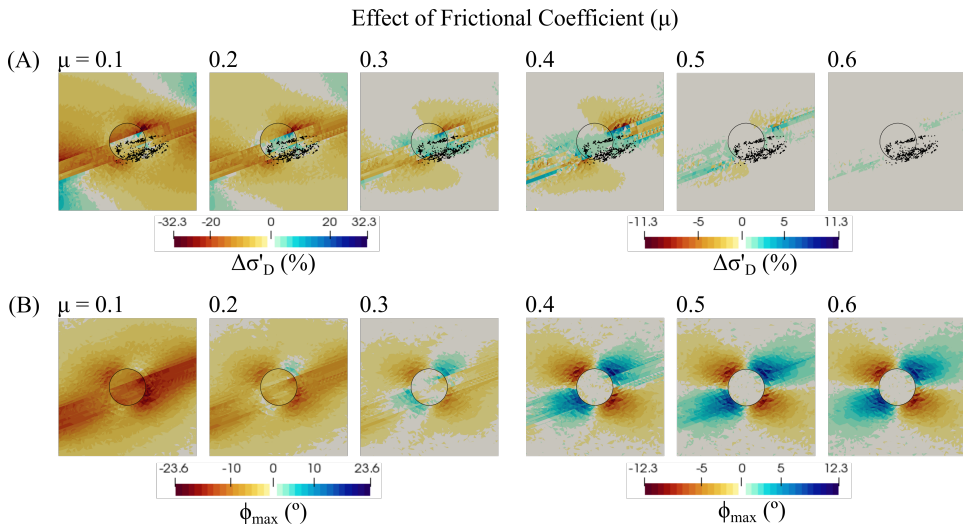


**Figure 11.** Effect of friction coefficient on the  $\Delta\sigma'_D$  and  $\phi_{\max}$  in the SD70R25V model at 10 km depth. Note the change in scale for  $\mu$  greater than 0.3. Earthquakes within 2 km of each depth slice are represented by black dots in 11A. <sup>OF:</sup>The outline of the impact structure is represented as black circle. Each figure is 70 × 70 km.

$\phi_{\max}$  maps show a clockwise stress rotation in the entire seismic zone, including the <sup>OF:</sup>eraterimpact structure region, when  $\mu$  values are 0.1 and 0.2 (Fig. 11B). When  $\mu$  is 0.3,  $\phi_{\max}$  is subparallel to the regional stress orientation within the <sup>OF:</sup>eraterimpact

379 structure region and the four-lobe pattern appears. For  $\mu \geq 0.4$ , the distribution of  $\phi_{\max}$   
 380 approaches that of the reference model.

### 381 3.5 Effects of velocity models

382 LD70R25 and TD70 are the same as SD70R25 except that they use different ve-  
 383 locity models. We use the 1D velocity model (Lamontagne, 1999) (Fig. 3) and the 3D  
 384 tomography results (Powell & Lamontagne, 2017) (Fig. 4) in LD70R25 and TD70 mod-  
 385 els, respectively. The  $V_p$  and  $V_s$  tomography model covers and extends beyond the OF:eraterim-  
 386 pact structure region, so the OF:eraterimpact structure-crust elastic moduli ratio is ir-  
 387 relevant because it is dictated by the velocities.

#### 388 3.5.1 LD70R25

389 Despite the difference in the 1D velocity models of Lamontagne (1999) and Somerville  
 390 et al. (1990) especially at depths shallower than 20 km (Fig. 3), the results of LD70R25  
 391 are similar in spatial distribution and in magnitude to those of SD70R25 (Fig. 12A). Re-  
 392 gions of positive  $\Delta\sigma'_D$  spatially overlap with the observed seismicity at all depths and  
 393 especially well at 10 km depth (Fig. 12A).

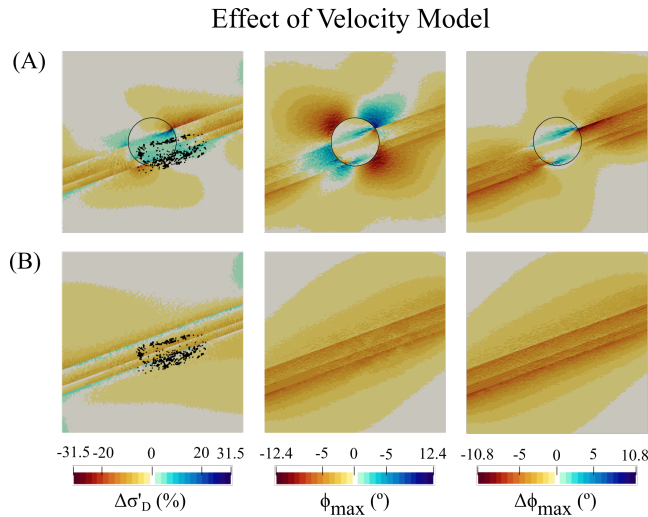


**Figure 12.** Same as Fig. 8 but only at a depth of 10 km for (A) LD70R25 and (B) TD70.

394 The  $\phi_{\max}$  maps also show the four-lobe pattern around the weaker OF:eraterimpact  
 395 structure and modification of the  $\phi_{\max}$  by the rift faults is observed (Fig. 12A). The max-

imum value of  $\phi_{\max}$  is  $21.7^\circ$  and decreases to  $12.4^\circ$  at 10 km depth. The  $\Delta\phi_{\max}$  map shows that the rotation of the reference model  $\phi_{\max}$  due to the rift faults is up to  $10.8^\circ$  at 10 km depth (Fig. 12A).

### 399      3.5.2 TD70

400      TD70 shows very different results from those of the models with a layered veloc-  
 401      ity model and a weak *OF:eraterimpact structure*. As the tomography model does not clearly  
 402      show low velocities within the *OF:eraterimpact structure* region,  $\Delta\sigma'_D$ ,  $\phi_{\max}$  and  $\Delta\phi_{\max}$   
 403      are all very similar to those in SD70R100, in which the *OF:eraterimpact structure* is not  
 404      distinguished from the surrounding crust in terms of elastic stiffness.

405      The spatial correlation between  $\Delta\sigma'_D$  and the observed seismicity is poor, especially  
 406      at 10 km depths (Fig. 12B). Below 15 km depths, the earthquakes fall within a region  
 407      of positive  $\Delta\sigma'_D$  but the modeled distribution of  $\Delta\sigma'_D$  predicts earthquakes throughout  
 408      the entire length of the rift faults.

409      The  $\phi_{\max}$  maps do not show the characteristic four-lobe pattern as seen in the mod-  
 410      els with the *OF:eraterimpact structure* due to the lack of a significant decrease in the ve-  
 411      locity model within the *OF:eraterimpact structure* versus outside the *OF:eraterimpact struc-*  
 412      *ture* (Fig. 12B). The  $\phi_{\max}$  maps show a clockwise rotation relative to the regional stress  
 413      orientation up to  $12.4^\circ$  at 10 km depth (Fig. 12B).

414      The  $\Delta\phi_{\max}$  is similar in magnitude and in spatial distribution with the  $\phi_{\max}$  maps  
 415      (Fig. 12B). This similarity in magnitude shows that the stress rotations in TD70 model  
 416      are due to the presence of the rift faults.

## 417      4 Discussions

### 418      4.1 Earthquake distribution

419      Our models suggest that having both the rift faults and the impact *OF:eraterstruc-*  
 420      *ture* is not only sufficient but also necessary for explaining the distribution of earthquakes  
 421      in the CSZ. The models without a weaker *OF:eraterimpact structure* zone, SD70R100 and  
 422      TD70, show regions of positive  $\Delta\sigma'_D$ , a proxy for earthquake generation potential, along  
 423      the entire length of the rift faults (e.g., Fig. 10B). In contrast, when the *OF:eraterimpac-*  
 424      *structure* is set to be *OF:less elastically stiff elastically softer* than the surrounding crust,

positive  $\Delta\sigma'_D$  regions spatially coincide with the observed seismicity in the CSZ, especially above 15 km depth (e.g., Fig. 6C). Our models predict that earthquake activity should extend to about 20 km *OF:distance* from the *OF:eraterimpact structure* in a north-east direction (Fig. 6C). This distribution of positive  $\Delta\sigma'_D$  is not seen in the reference model without the rift faults. These two findings from our models are consistent with the conclusion drawn by Thomas and Powell (2017) that the seismicity in CSZ requires both the damaged *OF:eraterimpact structure* zone and the rift faults.

The SD70R25 and SD65R25 models can explain the seismicity of the CSZ at least partially (Figs. 7 and 9). Correlation between the  $\Delta\sigma'_D$  distribution in SD65R25 and the observed seismicity shows a better and fine-scale correlation than in SD70R25, especially well near and within the *OF:eraterimpact structure* region (Fig. 9) while those in SD70R25 fit the observed seismicity better in the northeast region outside the *OF:eraterimpact structure* (Fig. 7). These differential correlations with seismicity of positive  $\Delta\sigma'_D$  regions in SD70R25 and SD65R25 might be suggesting along-strike variations in the dip angles of the rift faults (e.g., Baird et al., 2010). The SD65R25 model explains the observed seismic gap between the NW and SE clusters (i.e., between Gouffre Northwest and the Saint-Laurent faults, Fig. 1) and can also explain the rimming of earthquakes around the *OF:eraterimpact structure* as noted by Powell and Lamontagne (2017) especially at 10 km depth (Fig. 9).

Our present models, however, cannot explain the differences in earthquake activity between the *OF:eraterimpact structure* and the surrounding crust in the CSZ. ‘b’ values of the Gutenberg-Richter relationship for the regions within and outside the *OF:eraterimpact structure* are 0.93 and 0.74, respectively (Yu et al., 2016), indicating a higher frequency of small magnitude earthquakes within the *OF:eraterimpact structure*. Also, *OF:the large-magnitude most M4+* earthquakes in the CSZ *OF:occurred* appear to occur in the northeast region outside the *OF:eraterimpact structure* (e.g., Baird et al., 2010; Lamontagne, 1999; Powell & Lamontagne, 2017). *OF:Reexamination of historical earthquakes in the Charlevoix area by Stevens (1980)* *OF:shows that some M4+ earthquakes of the period 1924-1978 also occurred at the SE end of the impact structure.* Our models do not show significantly higher values of  $\Delta\sigma'_D$  in the seismogenic zone outside the *OF:eraterimpact structure* relative to the regions within the impact *OF:eraterstructure* (Fig. 6C). A possible explanation is that faults created in the highly fractured *OF:eraterimpact structure* region (Rondot, 2000) might have lower friction coefficients than the faults outside the *OF:eraterimpact structure*. Stress build-up on those weaker *OF:eraterimpact structure*

458 faults can be quicker and smaller in magnitude than on faults outside the *OF:eraterimpact-*  
 459 *structure* under the same tectonic loading, resulting in more numerous, smaller mag-  
 460 nitude earthquakes within versus outside the *OF:eraterimpact structure*.

#### 461 4.2 Spatial variations of $\text{SH}_{\max}$ orientation

462 Stress orientations in the CSZ from focal mechanism stress inversions (Mazzotti  
 463 & Townend, 2010; Zoback, 1992) show relative clockwise rotations within the CSZ and  
 464 in the CSZ relative to the regional stress orientation. A clockwise rotation of about  $47^\circ$   
 465 is observed in the SE relative to NW clusters of earthquakes and about  $32^\circ$  from the stress  
 466 inversion of the entire CSZ earthquakes relative to the  $\text{SH}_{\max}$  determined from borehole  
 467 breakouts (Mazzotti & Townend, 2010; Zoback, 1992) (Fig. 1).

468 Most of the earthquakes in the NW cluster are within the *OF:eraterimpact struc-*  
 469 *ture* region and occur at about 10 km depth (Fig. 1). Our model shows that the rift faults  
 470 tend to rotate the stress orientation clockwise in the upper 15 km depth but the amount  
 471 of rotation is reduced within the weak *OF:eraterimpact structure* (e.g., Fig. 6D). How-  
 472 ever, the model with a *OF:eraterimpact structure*-crust moduli ratio of 1.0 shows signif-  
 473 icant clockwise rotations uniformly along the entire length of the rift faults (Fig. 10B).  
 474 This observation suggests that the impact *OF:eraterstructure* tends to align the  $\phi_{\max}$  to  
 475 the regional tectonic loading direction within the *OF:eraterimpact structure*, particularly  
 476 at 10 km depth (Fig. 6D).

477 In a model with a *OF:eraterimpact structure* and the rift faults (SD70R25), the stress  
 478 rotation in the CSZ is clockwise (maximum value of  $20.3^\circ$ ) and decreases to  $0^\circ$  at an av-  
 479 erage of 20 km away from the CSZ (Fig. 6B). SD70R25 can explain about 60% of the  
 480  $32^\circ$  clockwise stress rotation observed in the CSZ relative to the borehole breakouts, and  
 481 about 43% of the  $47^\circ$  rotation in the SE part of the CSZ relative to the NW part. The  
 482 magnitudes of  $\phi_{\max}$  in the SD65R25 model are higher than the SD70R25 model by  $6^\circ$ ,  
 483 but show a small clockwise rotation within the *OF:eraterimpact structure* at 10 km depth,  
 484 and thus can explain about 80% of the  $32^\circ$  clockwise stress rotation observed in the CSZ  
 485 relative to the borehole breakouts, and about 55% of the  $47^\circ$  rotation in the SE part of  
 486 the CSZ relative to the NW part. The increase in  $\phi_{\max}$  in the SD65R25 relative to the  
 487 SD70R25 models suggests that the remaining observed stress rotations, not explained

488 by ~~OF: both models either model~~, could be partly due to change in dip angle of the rift faults  
 489 with depth.

490 A clockwise stress rotation of about  $44^\circ$  relative to the stress orientation from bore-  
 491 hole breakouts is also observed in the Lower St Lawrence seismic zone (Mazzotti & Tow-  
 492 nend, 2010). The Lower St. Lawrence seismic zone is located along the St. Lawrence River  
 493 to the NE of the CSZ, and does not contain an impact ~~OF: crater structure~~, similar to the  
 494 SD70R100 model. The rotation suggests that the presence of the rift faults and the rel-  
 495 ative angles of their strikes with respect to the regional orientation of  $\text{SH}_{\max}$  alone can  
 496 result in stress rotations (e.g., Zoback, 1992). However, the combined effect of the im-  
 497 pact ~~OF: crater structure~~ with up to a quarter of the elastic moduli of the surrounding crust,  
 498 and the rift faults are required in the CSZ to explain the observed clockwise rotations  
 499 of the  $\phi_{\max}$  in the SE cluster of earthquakes relative to the NW cluster, as well as in the  
 500 entire CSZ relative to the direction of regional tectonic loading.

### 501 4.3 Frictional strengths of the rift faults

502 The surface expression of the rift faults used in this study correspond to the Gouf-  
 503 fre Northwest Fault, Saint-Laurent fault and Charlevoix Fault (Fig. 1). We did not con-  
 504 sider the South Shore fault given its aseismic nature and ~~OF: its location at the extreme east-~~  
 505 ~~ern edge of the crater it appears to mark a boundary to the active zone~~ (Lamontagne,  
 506 1999). Our models show that a  $\mu$  of 0.3 and cohesion values of 0 MPa create  $\Delta\sigma'_D$  maps  
 507 that spatially correlate with the seismicity of CSZ and the observed stress rotations (Fig.  
 508 11). ~~OF: A  $\mu$  of 0.4 could also be suitable for the rift faults as the  $\Delta\sigma'_D$  maps also spa-~~  
 509 ~~tially correlate with the seismicity of CSZ, and some earthquakes also occurred at~~  
 510 ~~the SW region outside the impact structure (Fig. 1). However, previous works in the~~  
 511 ~~CSZ agreed with a finite extent of the seismic zone~~ (e.g., Stevens, 1980). ~~OF: This~~  
 512 ~~Our fault model~~ is different from the work of Baird et al. (2010) who modeled the Gouffre  
 513 Northwest Fault, Saint-Laurent fault and South Shore Fault (Fig. 1).

514 The fault parameters in our study are not compatible with the analysis of Hurd  
 515 and Zoback (2012a, 2012b) who suggest normal values of  $\mu$  ( $0.6 - 0.8$ ) for the rift faults  
 516 and hydrostatic pore pressure. Also, Fereidoni and Atkinson (2014) use Coulomb stress  
 517 theory to investigate stress change in the CSZ caused by the 1663 earthquake (moment  
 518 magnitude M of 7) and conclude that the rift faults are strong with  $\mu$  of 0.8. Fereidoni

519 and Atkinson (2014) showed that decreasing the apparent coefficient of friction reduces  
 520 the spatial correlation of the regions with enhanced stress and observed seismicity. Specif-  
 521 ically,  $\mu$  values of 0.2 and 0.4 give 66% and 75% spatial correlation, respectively. How-  
 522 ever, in our model, the regions of positive  $\Delta\sigma'_D$  significantly decrease in spatial extent  
 523 when  $\mu$  is 0.6, and do not fit the observed seismicity in the CSZ (Fig. 11).

524 *<sup>OF:</sup>In contrast to the normal faults as suggested by* Fereidoni and Atkinson (2014); Hurd  
 525 and Zoback (2012a, 2012b), Baird et al. (2010) *<sup>OF:</sup>conclude that the rift faults in the CSZ*  
 526 *are very weak with a friction angle of 5° that is equivalent to a  $\mu$  of about 0.1. This very low value*  
 527 *of  $\mu$  was necessary for their stopping criterion for boundary loading, which was  $\sigma_D$  equal to 200*  
 528 *MPa at 10 km depth.* In our study, we stop increasing boundary displacements when  $\sigma_D$   
 529 reaches 706 MPa at 10 km depth as described earlier without making any assumptions  
 530 for the intermediate principal stress ( $\sigma_2$ ). *<sup>OF:</sup>In contrast,* Baird et al. (2010) *<sup>OF:</sup>used a*  
 531  *$\sigma_D$  equal to 200 MPa at 10 km depth as their stopping criterion for boundary loading.*  
 532 *They suggested that the rift faults in the CSZ are very weak with a  $\mu$  of about 0.1. The*  
 533 *higher stopping criterion in our study is based on Byerlee's law under the assumption*  
 534 *of no pore-fluid pressure on the rift faults, and it is necessary to make faults slip at*  
 535 *seismogenic depth. Inclusion of pore-fluid pressure can significantly reduce the magni-*  
 536 *tude of  $\sigma_D$  used as the stopping criterion.* The stopping criteria of a  $\sigma_D$  of 200 MPa  
 537 at 10 km depth would not make rifts faults with  $\mu \geq 0.3$  slip *<sup>OF:</sup>at seismogenic depth*  
 538 *unless high pore fluid pressures are present. Other possible consequences of pore-fluid*  
 539 *pressure is that faults could be reactivated at smaller angles from the maximum com-*  
 540 *pressive stress* (e.g., Chen & Chen, 2018).

#### 541 4.4 Velocity model of the CSZ

542 Our models show that a 1D velocity model of the CSZ (Lamontagne, 1999) (Fig.  
 543 3) with embedded *<sup>OF:</sup>eraterimpact structure* and rift faults can explain the observed seis-  
 544 micity and more than 50% of the stress rotations (Fig. 12A). Using the velocity model  
 545 of the *<sup>OF:</sup>SanguenaySaguenay* region does not improve this result (Fig. 6). Similarly,  $\Delta\sigma'_D$   
 546 in the TD70 model did not spatially fit the recorded earthquakes in the upper 10 km in  
 547 the CSZ because the distinct and lower-strength damaged zone is not apparent in the  
 548 3D tomography (Powell & Lamontagne, 2017) (Fig. 12B). Lamontagne (1999) *<sup>OF:</sup>Fur-*  
 549 *ther investigation is needed to determine why the supposedly better velocity models failis a 1-D*

550 velocity model for the Canadian Shield region that does not include lateral variations  
 551 of velocity model to explain the seismicity and stress orientations.

552 **4.5 Limitations of our study**

553 Our models could not explain some earthquakes in the SW part of the *OF: crater impact*  
 554 structure especially in the upper 10 km depth (Fig. 6C). We did not account for  
 555 stress changes due to a large historic earthquake in the CSZ and the postglacial rebound  
 556 as modeled by Fereidoni and Atkinson (2014) and Mazzotti, James, Henton, and Adams  
 557 (2005), respectively.

558 Our models can only explain about 50% of the observed  $SH_{max}$  rotation. A pos-  
 559 sible hypothesis for the remaining stress rotation is a change in the dip of the rift faults  
 560 with depth and the effect of postglacial rebound. *OF: The high stress rotation could also be*  
 561 *due to unconstrained focal mechanisms used in the stress inversion.* Most of the focal mech-  
 562 anisms used for stress inversion *OF: in the CSZ* are obtained from first motion P and SH  
 563 waves (Lamontagne, 1998; Mazzotti & Townend, 2010). *OF: Better constrained* The focal mech-  
 564 anisms *OF: are good, and we suggest that the focal mechanisms can be further con-*  
 565 *strained* using waveform modeling *OF: will be needed* to validate the magnitude of the stress  
 566 rotation.

567 We *OF: simplified assumed that* the rift faults to be planar however, the fault *OF: trace traces*  
 568 on the geologic map of the CSZ *OF: is not straight are not linear* (Fig. 1). The scatter of  
 569 the seismicity within the *OF: crater impact structure* indicates that the faults do not re-  
 570 main planar. Future models depicting a more realistic fault geometry may also shed light  
 571 on the factors controlling stress rotation. Our model also did not incorporate pore pres-  
 572 sure which could have affected the calculated  $\mu$  *OF: and maximum  $\sigma_D$ .* The 3D veloc-  
 573 ity model is not *OF: accurate every well defined* in the upper 5 km depth and does not cover  
 574 the entire seismic zone (Fig. 4).

575 **5 Conclusions**

576 Findings from this study can be summarized as follows:

- 577 • The combined effects of the impact *OF: crater impact structure* and the rift faults  
 578 are required in the CSZ to explain the observed distribution of seismicity and more

579 than 50% of the observed clockwise rotations of the  $\phi_{\max}$  in the CSZ *OF:in respect*  
 580 *to the regional maximum compressive stress direction.*

- 581 • *OF:A-crater*An impact structure elastically weaker than the surrounding crust by  
 582 up to a factor of 4 is required to explain the seismicity in the upper 10 km of the  
 583 CSZ and the observed clockwise rotation of the  $\text{SH}_{\max}$  in the SE relative to the  
 584 NW part of the *OF:eraterimpact structure*. Below 10 km depth in the *OF:eraterim-*  
 585 *pact structure*, reactivation of the rift faults explains the observed seismicity in  
 586 the CSZ.
- 587 • Stress models that spatially correlate with the seismicity of CSZ and the observed  
 588 stress rotations were obtained when rifts faults have a friction coefficient of 0.3 and  
 589 zero cohesion *OF:under an assumption of no pore-fluid pressure on the rift faults.*
- 590 • The magnitudes of  $\text{SH}_{\max}$  rotation are greater in the  $65^{\circ}$ - $40^{\circ}$ - $40^{\circ}$  fault dip case  
 591 than the constant  $70^{\circ}$  fault dip case by  $6^{\circ}$ . The remaining  $\text{SH}_{\max}$  rotation could  
 592 be due to a change in the dip of the rift faults with depth.
- 593 • Stress models with dips of  $65^{\circ}$ ,  $40^{\circ}$  and  $40^{\circ}$  based on a recent hypocenter reloca-  
 594 tion study show a better correlation between the high differential stress regions  
 595 and the observed seismicity near and within the *OF:eraterimpact structure* region  
 596 than those with a constant  $70^{\circ}$  dip. However, the constant-dip models fit the ob-  
 597 served seismicity better in the northeast region outside the *OF:eraterimpact struc-*  
 598 *ture*. The partial success of each model might indicate more complex geometry  
 599 of the faults: e.g., an along-strike variation of the dip angles of the rift faults.

## 600 Acronyms

601 **CSZ** Charlevoix Seismic Zone

602 **SH**<sub>max</sub> Maximum horizontal principal stress

## 603 Acknowledgments

604 This project is supported by the National Science Foundation (NSF - ICER) under the  
 605 award title “EarthCube Building Blocks: Collaborative Proposal: GeoTrust: Improv-  
 606 ing Sharing and Reproducibility of Geoscience Applications” with an award number 1639706.  
 607 We acknowledge the high performance computing (HPC) resource center at the Univer-  
 608 sity of Memphis, TN for providing the computing time for this research. *OF:Earthquake*

609 hypocenters are available from Earthquakes Canada, GSC, Earthquake Search (On-line  
 610 Bulletin), <http://earthquakescanada.nrcan.gc.ca/stndon/NEDB-BNDS/bulleng.php>, Nat-  
 611 ural Resources Canada (1/30/2019).

612 **References**

- 613 Aagaard, B., Kientz, S., Knepley, M., Strand, L., & Williams, C. (2015). PyLith  
 614 User Manual, Version 2.1.0. *Computational Infrastructure of Geodynamic,*  
 615 *Davis, CA.*
- 616 Aagaard, B., Williams, C., & Knepley, M. (2015a). PyLith v2.1.0 [software]. *Compu-*  
 617 *tational Infrastructure for Geodynamics.*
- 618 Aagaard, B., Williams, C., & Knepley, M. (2015b). PyLith v2.1.0 [software]. *Com-*  
 619 *putational Infrastructure for Geodynamics.*
- 620 Anglin, F. (1984). Seismicity and faulting in the Charlevoix zone of the St. Lawrence  
 621 Valley. *Bulletin of the Seismological Society of America*, 74 (2): 595–603.
- 622 Baird, A. F., McKinnon, S. D., & Godin, L. (2010). Relationship between structures  
 623 stress and seismicity in the Charlevoix seismic zone revealed by 3-D geome-  
 624 chanical models: Implications for the seismotectonics of continental interiors.  
 625 *Journal of Geophysical Research*, 115(B11). doi: 10.1029/2010jb007521
- 626 Byerlee, J. (1978). Friction of rocks. *Pure and Applied Geophysics PAGEOPH*,  
 627 116(4-5), 615–626. doi: 10.1007/bf00876528
- 628 Chen, S., & Chen, Z. (2018). On the reactivation of the pre-existing normal fault.  
 629 *World Journal of Mechanics*, 8(5), 210-217. doi: 10.4236/wjm.2018.85016
- 630 Fereidoni, A., & Atkinson, G. M. (2014). Correlation between coulomb stress  
 631 changes imparted by historic earthquakes and current seismicity in charlevoix  
 632 seismic zone, eastern canada. *Seismological Research Letters*, 86(1), 272. doi:  
 633 10.1785/0220140134
- 634 Gardner, G. H. F., Gardner, L. W., & Gregory, A. R. (1974). Formation veloc-  
 635 ity and density—the diagnostic basics for stratigraphic traps. *GEOPHYSICS*,  
 636 39(6), 770–780. doi: 10.1190/1.1440465
- 637 Hurd, O., & Zoback, M. D. (2012a). Intraplate earthquakes, regional stress and fault  
 638 mechanics in the central and eastern u.s. and southeastern canada. *Tectono-*  
 639 *physics*, 581, 182 - 192. (Crustal Stresses, Fractures, and Fault Zones: The  
 640 Legacy of Jacques Angelier) doi: <https://doi.org/10.1016/j.tecto.2012.04.002>

- 641 Hurd, O., & Zoback, M. D. (2012b). Regional stress orientations and slip compatibility  
642 of earthquake focal planes in the new madrid seismic zone. *Seismological*  
643 *Research Letters*, 83(4), 672. doi: 10.1785/0220110122
- 644 Lamontagne, M. (1998). New and revised earthquake focal mechanisms for the  
645 Charlevoix Seismic Zone, Canada. *Geological Survey of Canada. Open File,*  
646 *OF3556*.
- 647 Lamontagne, M. (1999). Rheological and geological constraints on the earthquake  
648 distribution in the Charlevoix Seismic Zone, Quebec, Canada. *Geological Sur-*  
649 *vey of Canada. Open File, D3778*.
- 650 Marone, C. (1995). Fault zone strength and failure criteria. *Geophysical Research*  
651 *Letters*, 22(6), 723-726. doi: 10.1029/95GL00268
- 652 Mazzotti, S., James, T. S., Henton, J., & Adams, J. (2005). GPS crustal strain,  
653 postglacial rebound, and seismic hazard in eastern north america: The saint  
654 lawrence valley example. *Journal of Geophysical Research: Solid Earth*,  
655 110(B11). doi: 10.1029/2004JB003590
- 656 Mazzotti, S., & Townend, J. (2010). State of stress in central and eastern North  
657 American seismic zones. *Lithosphere*, 2(2), 76–83. doi: 10.1130/l165.1
- 658 Powell, C. A., & Lamontagne, M. (2017). Velocity models and hypocenter reloca-  
659 tions for the Charlevoix Seismic Zone. *Journal of Geophysical Research: Solid*  
660 *Earth*, 122(8), 6685–6702. doi: 10.1002/2017jb014191
- 661 Rondot, J. (1971). Impactite of the Charlevoix Structure Quebec, Canada. *Journal*  
662 *of Geophysical Research*, 76(23), 5414–5423. doi: 10.1029/jb076i023p05414
- 663 Rondot, J. (1994). Recognition of eroded astroblemes. *Earth-Science Reviews*,  
664 35(4), 331 - 365. doi: 10.1016/0012-8252(94)90001-9
- 665 Rondot, J. (2000). Charlevoix and sudbury as gravity-readjusted impact struc-  
666 tures. *Meteoritics & Planetary Science*, 35(4), 707-712. doi: 10.1111/j.1945  
667 -5100.2000.tb01454.x
- 668 Somerville, P. G., McLaren, J. P., Saikai, C. K., & Helmberger, D. V. (1990). The  
669 25 November 1988 Saguenay, Quebec, Earthquake: Source Parameters and the  
670 Attenuation of Strong Ground Motion. *Bulletin of the Seismological Society of*  
671 *America*, 80.
- 672 Stevens, A. E. (1980). Reexamination of some larger La Malbaie, Québec, earth-  
673 quakes (1924-1978). *Bulletin of the Seismological Society of America*, 70(2),

- 674 529-557.
- 675 Thomas, W. A., & Powell, C. A. (2017). Necessary conditions for intraplate  
676 seismic zones in north america. *Tectonics*, 36(12), 2903-2917. doi:  
677 10.1002/2017TC004502
- 678 Vlahovic, G., Powell, C., & Lamontagne, M. (2003). A three-dimensionalPwave ve-  
679 locity model for the Charlevoix seismic zone Quebec, Canada. *Journal of Geo-*  
680 *physical Research: Solid Earth*, 108(B9). doi: 10.1029/2002jb002188
- 681 Yu, H., Liu, Y., Harrington, R. M., & Lamontagne, M. (2016). Seismicity along  
682 st. lawrence paleorift faults overprinted by a meteorite impact structure in  
683 charlevoix, québec, eastern canadaseismicity along st. lawrence paleorift faults  
684 overprinted by a meteorite impact structure in charlevoix. *Bulletin of the*  
685 *Seismological Society of America*, 106(6), 2663. doi: 10.1785/0120160036
- 686 Zoback, M. L. (1992). First- and second-order patterns of stress in the lithosphere:  
687 The World Stress Map Project. *Journal of Geophysical Research*, 97(B8),  
688 11703. doi: 10.1029/92jb00132